Ceramics International 49 (2023) 36791–36799

Contents lists available at ScienceDirect

Ceramics International

journal homepage: www.elsevier.com/locate/ceramint

Mn^{2+}-doped $MgGeO_3$ nanophosphors with controlled shape and optimized persistent luminescence

Daniel González-Mancebo [1], Encarnación Arroyo [1], Ana Isabel Becerro [*], Manuel Ocaña [**]

Instituto de Ciencia de Materiales de Sevilla (ICMS), CSIC-US, c/Américo Vespucio, 49, 41092, Seville, Spain

ARTICLE INFO

Handling Editor: Dr P. Vincenzini

Keywords:
$MgGeO_3$
Manganese
Persistent luminescence
Nanophosphor
Salt-assisted

ABSTRACT

Mn^{2+}-doped $MgGeO_3$ ($MgGeO_3$:Mn^{2+}) is an efficient persistent phosphor that emits red luminescence for long time after stopping excitation with UV light. For optical and biotechnological uses a precise control of particle size and shape is highly desired since these parameters may have a strong influence on the properties and suitability of phosphor materials for the intended applications. To the best of our knowledge, $MgGeO_3$:Mn^{2+} has been synthesized by conventional solid-state-reaction, which yields particles of heterogeneous size and shape. Here, we report for the first time in the literature a salt-assisted method for the synthesis of $MgGeO_3$:Mn^{2+} nanoparticles with uniform shape (nanorods) and a mean size of 350 nm × 99 nm. The rigorous study of the luminescence properties of the $MgGeO_3$:Mn^{2+} nanorods revealed that whereas the optimum doping level for photoluminescence was 2.0 mol% Mn^{2+}, the best persistent luminescence was attained with just 0.5 mol% Mn^{2+}, which is ascribed to the different mechanisms of both luminescence processes. The optimum persistent nanophosphor showed an intense red emission, which persisted at least 17 h after stopping the excitation. Such excellent properties make the developed nanophosphor an attractive candidate for use in optical and biotechnological applications.

1. Introduction

Much attention has been paid in the last years to research involving persistent luminescence (PersL) materials [1–4]. This kind of phosphors emit light for extended periods of time (from minutes to days) after stopping the excitation radiation (near-infrared light, visible light, ultraviolet light, X-rays, electrons or gamma radiation) [3,5]. This phenomenon is due to the storage of excitation energy in intrinsic traps (holes or electrons) and the further release of the trapped charges, which produce the emission of photons under proper (mainly thermal) stimulation [2]. PersL materials are currently used in several areas of technology, the most popular being displays and safety signaling [1]. Their use for other novel applications such as photocatalysis [6], solar cells [7], anticounterfeiting [8], optical information storage [9], sensing [10], bioimaging [11], and therapy [12], has also been proposed. PersL materials are particularly interesting for bioapplications, as PersL phosphors are charged prior to injection into biological tissues, thus preventing tissues autofluorescence that usually occurs with conventional phosphors, resulting in higher signal to noise ratio of the images [11].

For many of these applications, a control of particle size and shape is highly desired since these parameters may have a strong influence on the properties and suitability of the phosphor materials for the intended applications. For example, for biological applications nanoparticulated materials with uniform shape and appropriate size (<200 nm) are required [3,11]. In addition, it is well known that for the preparation of films for optical applications, a very simple and economical method is spin-coating from colloidal suspensions, which must consist of nanoparticles (NPs) to achieve transparency and optical quality [13].

In 2003, Iwasaki et al. reported that Mn^{2+}-doped $MgGeO_3$ is an efficient persistent phosphor that emits red luminescence for long time after stopping excitation with UV light [14]. In this material, $MgGeO_3$ shows an orthorhombic pyroxene-type structure consisting of single chains of Ge^{4+} tetrahedra running parallel to the c-axis and two types of Mg^{2+} octahedral sites [15]. Due to their similar ionic radii and same oxidation state, Mn^{2+} substitutes Mg^{2+} in the $MgGeO_3$ crystal structure, as indicated by the red emission of the material under UV light, which is characteristic of Mn^{2+} in octahedral sites [16]. Since the pioneering

* Corresponding author.
** Corresponding author.
E-mail addresses: anieto@icmse.csic.es (A.I. Becerro), mjurado@icmse.csic.es (M. Ocaña).
[1] These authors had equal contributions.

https://doi.org/10.1016/j.ceramint.2023.09.008
Received 19 June 2023; Received in revised form 9 August 2023; Accepted 4 September 2023
Available online 5 September 2023

work by Iwasaki et al., some other papers on this phosphor have appeared, most of them aiming to increase the intensity and duration of the persistence luminescence by co-doping with different trivalent cations (bismuth, lanthanides) to modulate the emission features [17–20] or to explore their potential applications for optical information storage [20] or bioimaging [19,20]. In these works, the co-dopant content has been optimized to achieve maximum persistence. However, the effects of Mn^{2+} doping level on this magnitude has not been addressed to the best of our knowledge, which is surprising since this task is essential to optimize the persistence properties [4]. Moreover, in most previous works, the samples were synthesized through the conventional solid-state method, which requires high calcination temperatures leading to aggregation and sintering, thus precluding any control of the morphological properties of the obtained phosphor.

During the last decades, several salts-assisted methods for the synthesis of materials by solid-state reactions have been developed, which have been shown to be suitable to decrease the temperature of formation of the desired phase and/or to control the particle size and shape. Depending on the melting point of the salt, these methods are classified into molten-salt methods (with low melting point salts) [21–23], or salt-templated synthesis (with high melting point salts) [24,25]. In the first case, the salt melts during calcination favoring the dissolution of reagents and the diffusion processes required for phase formation, which eventually reduces the crystallization temperature [22]. This also affects to nucleation and particle growth processes and, therefore, a certain control on particle size and shape can be achieved [21]. When working at lower temperature than the melting point of the added salt, the later may act as template [25] or as dispersing agent to avoid particle growth and sintering [26], in both cases leading to different nanostructured materials. In these synthesis methods, the chosen salts must be water soluble so that they can be easily removed by washing after calcination.

Here, we report on the synthesis of Mn^{2+}-doped $MgGeO_3$ nanoparticles by using a salt-assisted method at temperatures below the melting point of the salt (K_2SO_4), which allows a certain control on particle size and shape for the first time in literature for this kind of PersL phosphor. The effects of Mn^{2+} doping level on the photoluminescence and persistent luminescence properties, which has not been reported yet for this system, are also evaluated aiming to optimize the nanophosphor performance.

2. Experimental

2.1. Reagents

Germanium (IV) oxide (GeO_2, Sigma Aldrich, ≥99.99%), magnesium carbonate hydroxide pentahydrate ($Mg_5(CO_3)_4(OH)_2{\cdot}5H_2O$, Sigma Aldrich), manganese (II) chloride ($MnCl_2$, Sigma Aldrich, ≥99%), potassium sulphate (K_2SO_4, Sigma Aldrich, ≥99.0%), phosphate buffered saline (PBS solution, pH 7.4, Sigma Aldrich) and hydrochloric acid (HCl, Sigma Aldrich, 37%) were used as received.

2.2. Synthesis procedures

Undoped $MgGeO_3$ particles were synthetized according to three different procedures (Scheme 1).

Method I In a typical synthesis, 0.30 mmol of GeO_2 were dissolved in 15 mL of double distilled water at 80 °C under magnetic stirring until the solution became completely transparent. The solution was then allowed to cool down. Next, K_2SO_4 (4.5 mmol) was dissolved in 15 mL of double distilled water and $Mg_5(CO_3)_4(OH)_2{\cdot}5H_2O$ (0.06 mmol) was added to the solution, which was magnetically stirred at room temperature (RT) for 5 min. A slight turbidity was observed, which may be due to the incomplete dissolution of the later compound. Both solutions were then admixed and homogenized under magnetic stirring at RT for 5 min. The final solution was poured into a crystallizer (11 cm diameter) and allowed to evaporate to dryness in a conventional oven preheated to 120 °C for 3 h. The obtained powder was gently ground in an agate mortar and annealed in a porcelain crucible at different temperatures (10 °C·min^{-1}) for 4 h. The resulting solid was washed with double distilled water to remove K_2SO_4.

Method II Following a solid-state reaction, GeO_2 (0.30 mmol), $Mg_5(CO_3)_4(OH)_2{\cdot}5H_2O$ (0.06 mmol) and K_2SO_4 (4.5 mmol) were mixed together and homogenized by grinding in an agate mortar during 10 min with addition of acetone. The as prepared powder was placed into a porcelain crucible and calcined at different temperatures for 4 h.

Method III This method involved the same experimental conditions described above for method I without the addition of K_2SO_4.

For the synthesis of Mn^{2+}-doped $MgGeO_3$ ($MgGeO_3$:Mn^{2+}) particles,

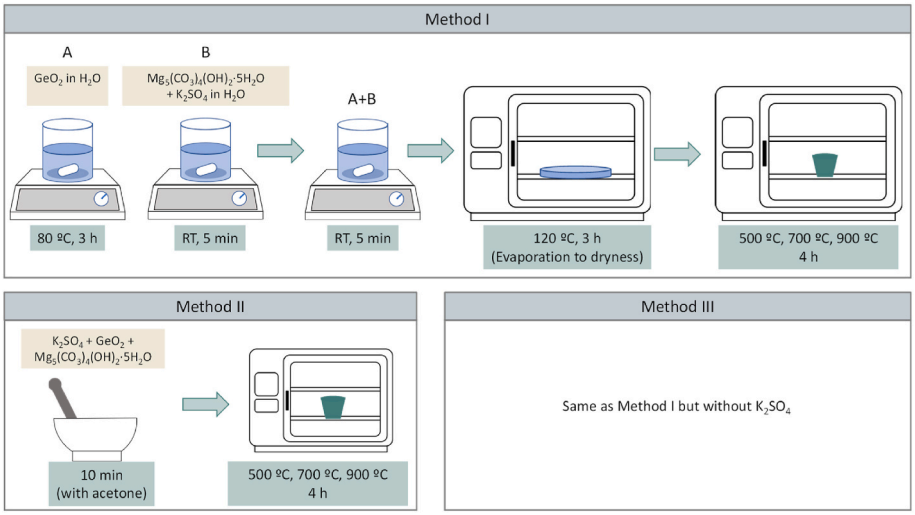

Scheme 1. Description of $MgGeO_3$ synthesis methods used in this study (RT = Room Temperature).

we used method I, but adding the desired amount of $MnCl_2$, from a concentrated solution, to the starting solution. Different doping levels, from 0.2 to 4.0 mol% Mn^{2+}, were assayed aiming to optimize the luminescent properties of the synthesized phosphors.

2.3. Characterization techniques

Transmission electron microscopy (*TEM,* JEOL2100Plus) and scanning electron microscopy (*SEM-FEG*, Hitachi S4800) were used to examine particle shape and size. The size distribution (fitted with a Gauss function) was obtained from the TEM images by counting several hundreds of particles using the free software *ImageJ*. High resolution transmission electron microscopy (*TEM,* JEOL2100Plus) was used to study the microstructure of the $MgGeO_3$:Mn^{2+} nanoparticles. The chemical composition of the particles was analysed under a TEM microscope (FEI TALOS S200) using energy dispersive X-ray spectroscopy (EDX) mappings.

Phase identification was carried out by X-ray powder diffraction (XRD) using a P'Analytical X'Pert Pro diffractometer (CuKα) with an X-Celerator detector over an angular range of $10° < 2\theta < 70°$, a 2θ step width of 0.05°, and 300 s counting time. Lattice parameters of the $MgGeO_3$:Mn^{2+} samples were determined from their XRD pattern by the Le-Bail method using PDF 00-034-0281 as starting parameters. The full width at half maximum of the (220) reflection (located around 35° 2θ) was used to calculate the crystallite size of the particles by using the Scherrer equation.

Fourier transform infrared (FTIR) spectra were recorded for powdered samples diluted in KBr pellets using a JASCO FT-IR-6200 Fourier transform spectrometer.

Inductively coupled plasma atomic emission spectroscopy (ICP-AES, Horiba Jobin Yvon, Ultima2) was used to determine the quantitative composition of the $MgGeO_3$:Mn^{2+} particles. For this purpose, powdered samples (~8 mg) were previously digested in hydrochloric acid (3 mL) with magnetic stirring for 3 h at RT.

The optical characterization of the $MgGeO_3$:Mn^{2+} samples was carried out in an Edinburgh FLS1000 spectrometer. For a quantitative comparison of the luminescent properties, a small hole (2 mm diameter, 0.5 mm depth), made in a quartz slide, was filled with the same mass of powdered samples, and then covered with a quartz lid. The excitation and emission spectra were recorded using wavelengths of 678 nm and 250 nm, respectively. All spectra were corrected for the optical system responses. For the measurement of persistent luminescence decay curves, the samples were previously excited for 5 min at 250 nm to charge the traps, and the decay curves were then monitored every 0.4 s at 678 nm after stoppage of the excitation. The excitation and emission slits were both set at 13 nm for maximizing the intensity. During excitation, an optical density filter (OD 3) was placed in the emission pathway to avoid detector saturation and it was quickly removed to record the persistent emission when the excitation was stopped. Persistent luminescence excitation spectra were obtained by integrating the first minute of the persistent luminescence decay curves, recorded at different wavelengths in the interval 250–400 nm. The integrated values were corrected by the lamp response at each wavelength and the sample was discharged by heating with a hair dryer after each experiment. Finally, persistent luminescence emission spectra were obtained by integration of the persistent luminescence decay curves (first minute), recorded after excitation at 250 nm at different detector positions (from 500 to 900 nm). The first two data points after switching off the UV light were discarded for integration of all persistent luminescence decay curves. Finally, persistent luminescence decay curves were also recorded in the same way as before but using a 639 nm laser (output power 200 mW).

Digital photographs were taken with a digital camera while illuminating the powdered samples (deposited by filtration on a 100 nm pore size Millipore filter) with both white light and UV light (conventional UV lamp at 312 nm). The same amount of powder was used for each sample so that the photographs could be compared to each other. The acquisition parameters were: manual-ISO 250–1/3 s.

Persistence images were acquired using an IVIS Lumina LT Series III equipment. Powdered samples were dispersed in PBS (pH = 7.4) at a concentration of 27 mg/mL and sonicated for 2 min. Then, 0.150 mL of each dispersion were placed in a Microplate 96 well (F Bottom, Black, Greiner. Bio-one). The microplate was subsequently illuminated with a conventional UV lamp (312 nm) for 5 min and the persistent luminescence signal was recorded at different times after stopping the UV illumination.

3. Results and discussion

3.1. Synthesis and characterization of undoped $MgGeO_3$ nanoparticles

$MgGeO_3$ nanoparticles were synthesized following method I (see Scheme 1 in Experimental section), which involves the admixture of Mg^{2+} and Ge^{4+} precursors and K_2SO_4 salt in water to ensure their intimate mixing followed by evaporation to dryness at 120 °C, and calcination at increasing temperatures (500, 700 and 900 °C). The sample obtained after each calcination was washed with double distilled water to facilitate its characterization by removal of the K_2SO_4 contribution.

The XRD pattern of the product obtained after drying at 120 °C (and washing to remove K_2SO_4) (Fig. 1a) indicated that the mixture of the precursors in water and further evaporation to dryness not only led to the intended intimate mixing of the precursors, but to a chemical reaction between Ge and Mg precursors. Thus, the XRD pattern matched with PDF 00-012-0063 which corresponds to a product obtained after prolonged boiling of K_2GeO_3 and $MgCl_2$ [27]. The authors observed that their diffraction pattern was very similar to that of a layered magnesium silicate obtained in the same conditions [28] and concluded that their product was a magnesium germanium oxide hydrate with a layered structure very similar to that of such magnesium silicate.

FTIR spectroscopy also supports the occurrence of a chemical reaction between the Ge and Mg precursors during the drying treatment at 120 °C. Thus, comparison of the FTIR spectrum of the sample dried at 120 °C with those of the Mg and Ge precursors (Fig. 2a) showed important variations in the position and relative intensity of the bands

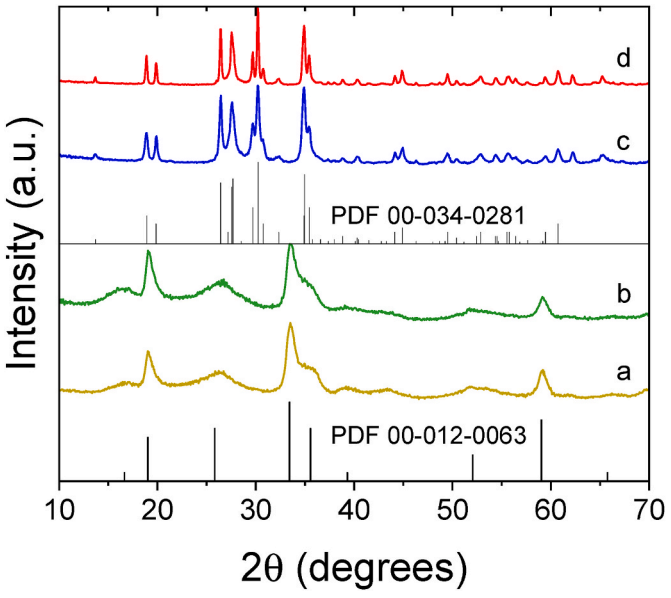

Fig. 1. Experimental XRD patterns of the sample obtained after evaporation to dryness of the precursor solution at 120 °C (following method I) (a) and of the powders obtained after calcination of such sample at 500 °C (b), 700 °C (c) and 900 °C (d). PDF 00-012-0063 (magnesium germanium oxide hydrate) and PDF 00-034-0281 (orthorhombic $MgGeO_3$) are also included.

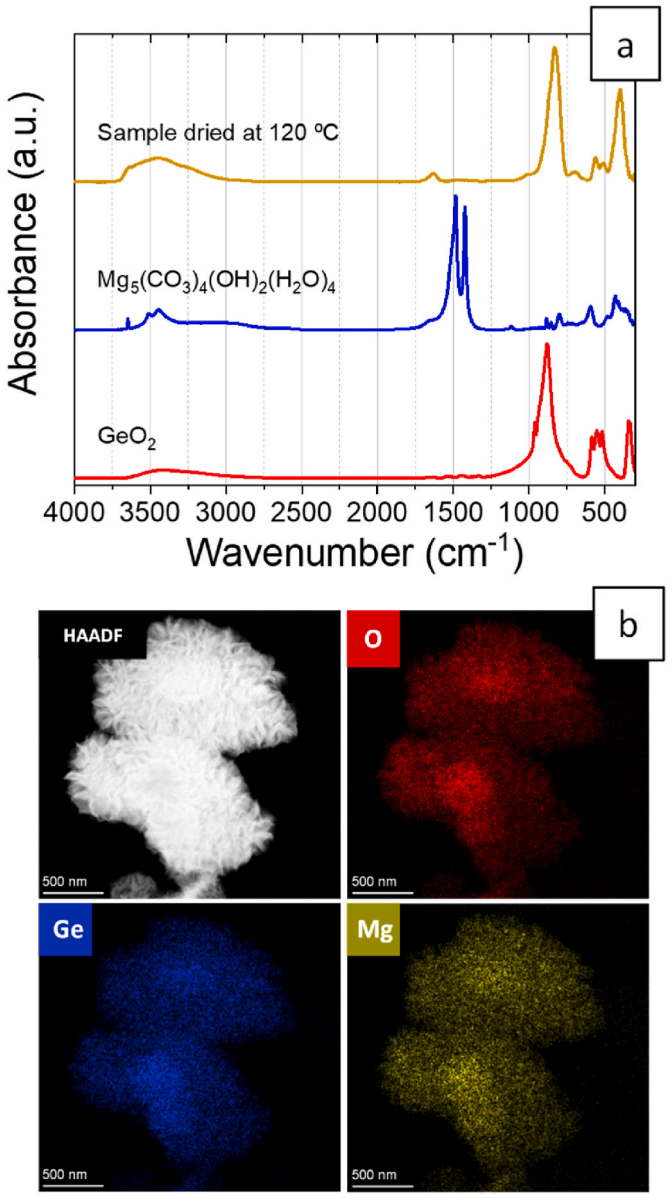

Fig. 2. a) FTIR spectra of the sample obtained after evaporation to dryness of the precursor solution at 120 °C (following method I) and of the Mg and Ge precursors. b) STEM-HAADF image and O, Ge, and Mg EDX mappings of the sample dried at 120 °C.

corresponding to the lattice (<1000 cm^{-1}) and OH (3700-3200 cm^{-1}) vibrations as well as the almost complete disappearance of the carbonate bands (~1500 cm^{-1}) corresponding to the Mg precursor. Finally, in agreement with the above findings, the EDX compositional mapping of the sample dried at 120 °C (Fig. 2b) showed the presence of Ge and Mg not segregated but intimately mixed within all the particles. We can, therefore, conclude that a chemical reaction between the germanium and magnesium precursors took place during their drying pretreatment at 120 °C giving rise to a magnesium germanium oxide hydrate with layered structure.

As revealed by XRD (Fig. 1b), no structural changes were detected after calcination of the dried product up to 500 °C while orthorhombic $MgGeO_3$ was completely formed at 700 °C (Fig. 1c). When the calcination temperature was increased from 700 to 900 °C (Fig. 1d), only a narrowing of the reflections was noticed, which indicates an increase of crystallite size (from 35 to 43 nm). It is outstanding that the formation temperature of $MgGeO_3$ following this synthesis method is much lower than that required to crystallize the phase through conventional solid-state reaction (SSR), which, according to literature [29] and our own experiments (Fig. S1), was ≥1100 °C. It should be noticed that such reduction of crystallization temperature cannot be ascribed to the processes associated to the molten salt method since, in our case, we work below the K_2SO_4 melting point (1065 °C) and therefore, a liquid phase is not present to favor the diffusion process required for crystallization [21–23]. To elucidate the reason for such important reduction in the formation temperature of the $MgGeO_3$ phase following method I, two separate sets of experiments were conducted. Firstly, the magnesium and germanium precursors and the K_2SO_4 salt were not dissolved in water previous to calcination, but they were just mixed in dried form and gently ground in an agate mortar in the presence of a small amount of acetone to favor homogenization (method II).

The XRD pattern obtained after calcination of this precursors mixture at 500 °C (Fig. 3a) showed several broad reflections that suggest a poorly crystallized phase probably coming from the decomposition of the starting magnesium carbonate hydroxide. A set of intense, narrow reflections corresponding to tetragonal GeO_2 (PDF 00-035-0729) and several tiny peaks corresponding to the incipient crystallization of $K_4Ge_9O_{20}$ (PDF 00-014-0157) were also present. After calcination at 700 °C, the XRD pattern (Fig. 3b) was characteristic of a well crystallized powder showing narrow and intense reflections corresponding to $K_4Ge_9O_{20}$ (PDF 00-014-0157). The pattern also showed several weak reflections of both $K_2Ge_4O_9$ (PDF 00-040-1188) and $MgGeO_3$ (marked with asterisks). Finally, the sample calcined at 900 °C (Fig. 3c) consisted mainly of $K_2Ge_4O_9$ (PDF 00-040-1188) and, in a much lower proportion, of $MgGeO_3$ (marked with asterisks) and Mg_2GeO_4 (marked with circles). Therefore, the full crystallization of $MgGeO_3$ is not observed at the highest calcination temperature (900 °C) following method II. This result indicates that the low crystallization temperature of $MgGeO_3$ observed following method I (700 °C) cannot be only due to the addition of K_2SO_4.

Secondly, the magnesium and germanium precursors were dissolved in double distilled water without adding the salt and the resulting solution was evaporated to dryness in a conventional oven at 120 °C for 3 h (method III).

The XRD pattern of the obtained product (Fig. 4a) was similar to that

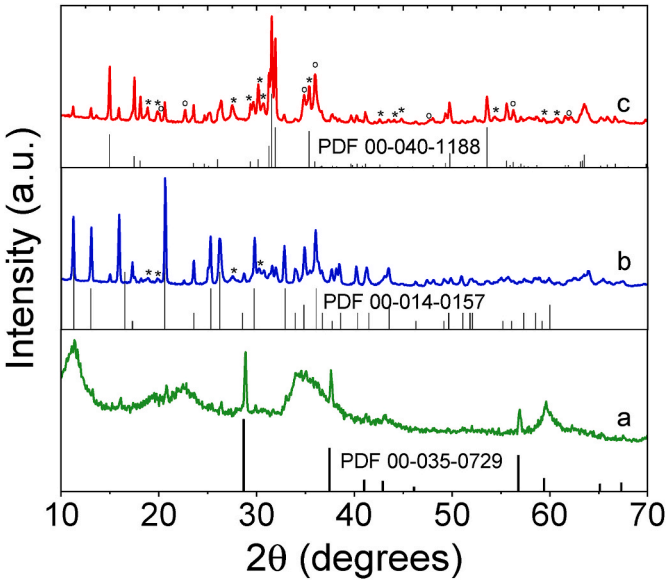

Fig. 3. Experimental XRD patterns of samples prepared by method II and annealed at 500 °C (a), 700 °C (b), and 900 °C (c). PDF 00-035-0729 = tetragonal GeO_2, PDF 00-014-0157 = tetragonal $K_4Ge_9O_{20}$, PDF 00-040-1188 = hexagonal $K_2Ge_4O_9$. Symbols: Asterisks = orthorhombic $MgGeO_3$ (PDF 00-034-0281), circles = orthorhombic Mg_2GeO_4 (PDF 00-036-1479).

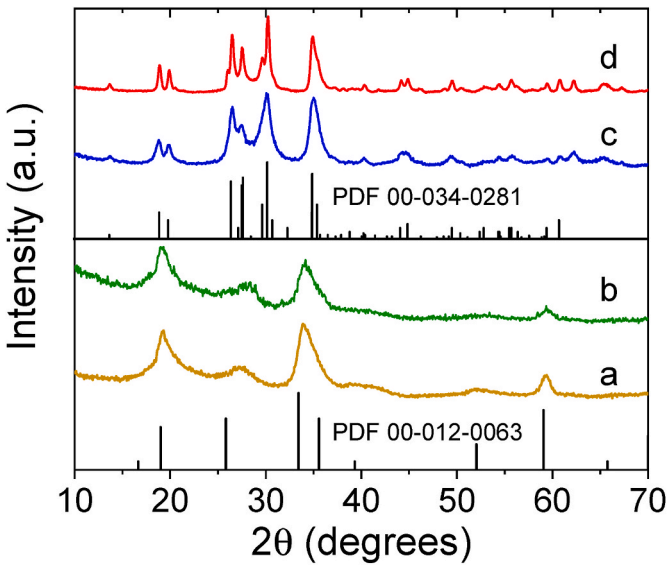

Fig. 4. Experimental XRD patterns of the sample obtained after evaporation to dryness of the precursor solution at 120 °C (following method III) (a) and of the powders obtained after calcination of such sample at 500 °C (b), 700 °C (c), and 900 °C (d). PDF 00-012-0063 (magnesium germanium oxide hydrate) and PDF 00-034-0281 (orthorhombic $MgGeO_3$) are also included.

resulting from method I, which consisted mainly of layered magnesium germanium oxide hydrate phase, although a lower degree of crystallinity (broader reflections) was observed in this case. The same XRD pattern was observed after calcination at 500 °C (Fig. 4b), while a phase transformation into the $MgGeO_3$ was inferred from the XRD pattern of the sample annealed at 700 °C (Fig. 4c). Therefore, the temperature necessary for the formation of $MgGeO_3$ following method III was the same temperature as for method I. This result reveals that the main factor responsible for the speeding of the $MgGeO_3$ crystallization is the formation, during the drying pretreatment at 120 °C, of the layered magnesium germanium oxide hydrate phase, in which the Mg and Ge cations are intimately mixed thus favoring the diffusion processes required for the crystallization of $MgGeO_3$. When the calcination temperature was further increased to 900 °C (Fig. 4d), a narrowing of the reflections was noticed, indicating an increase of crystallite size (14 nm at 700 °C and 29 nm at 900 °C). Irrespective of the calcination temperature, crystallite sizes were smaller than those obtained with salt addition (method I) indicating that a higher crystallinity was attained using method I.

The addition of salt had also a strong influence on the morphological features of the products as shown in the micrographs displayed in Fig. 5.

It can be observed that after drying the starting solutions at 120 °C, the product obtained in the absence of salt (method III) (Fig. 5a) consisted of lamellae organized into a sponge-like microstructure, whereas such hierarchical structure of lamellae was not detected when adding salt (method I) (Fig. 5d). It should be noticed that the observed lamellae are compatible with the formation of the layered magnesium germanium oxide hydrate as revealed by XRD in both methods (Figs. 1a and 4a). On calcination, the sponge-like microstructure obtained in the absence of salt was kept up to 900 °C (Fig. 5b and c). However, in the presence of salt, the starting lamellae transformed into small (<100 nm) crystallites at 700 °C (after $MgGeO_3$ formation) (Fig. 5e) and into well-defined nanorods, after calcination at 900 °C (Fig. 5f). The nanorods, with dimensions 350 ($\sigma = 100$) nm x 99 ($\sigma = 25$) nm (Fig. S2) exhibited a high degree of crystallinity, as revealed by the HRTEM micrograph (Fig. 6), which clearly showed bright fringes running parallel to the long axis of the rod. The fringes were spaced 4.68 Å, which corresponds to the (400) planes of the orthorhombic $MgGeO_3$ structure. This result indicates that the *a* axis of the orthorhombic $MgGeO_3$ unit cell was perpendicular to the large dimension of the rod.

In addition, it is worth mention that the microstructures shown above differ significantly from that observed after a conventional solid-state reaction (Fig. S3), which consists of sintered, irregular shape crystals.

In summary, all these findings reveal that the addition of K_2SO_4 to the starting solution of the magnesium and germanium precursors is essential to obtain $MgGeO_3$ nanoparticles with well-defined morphology. Although, the reason for the different particle size and shape caused by the addition of salt are not fully understood, it may be attributed to the different microstructure and crystallinity observed for the dried precursors, since these factors may affect to the nucleation and crystal growth processes taking place during calcination.

3.2. *Synthesis of Mn^{2+}-doped $MgGeO_3$ nanophosphors and study of their luminescent properties*

$MgGeO_3$ nanorods doped with different Mn^{2+} contents (nominal values from 0.2 up to 4.0 mol%) were synthesized following the salt-assisted method (method I) using a calcination temperature of 900 °C. The experimental Mn^{2+} contents were determined by ICP resulting close values to the nominal ones (Table 1), the differences have been ascribed to weighing errors. The samples will be named hereafter as $MgGeO_3$:x% Mn^{2+} where x stands for the nominal mol% Mn^{2+}. Fig S4 shows that the Mn^{2+} doping level did not alter either the size or the shape of the synthesized particles, all of which consisted of rods with approximate mean size 350 nm × 95 nm. However, the XRD patterns of the samples (Fig. 7a) showed a shift of the reflections towards lower 2θ angles with

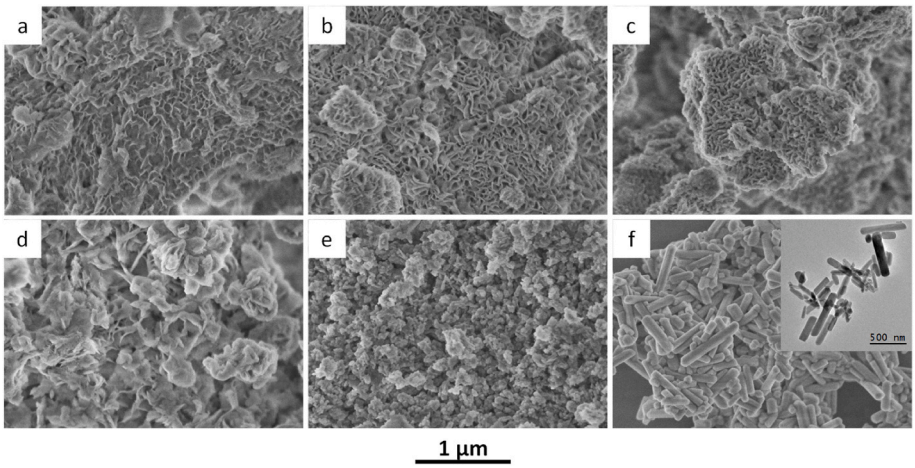

Fig. 5. Top: SEM micrographs of the sample obtained after evaporation to dryness of the precursor solution at 120 °C (following method III) (a) and of the powders obtained after calcination of such sample at 700 °C (b) and 900 °C (c). Bottom: SEM micrographs of the sample obtained after evaporation to dryness of the precursor solution at 120 °C (following method I) (d) and of the powders obtained after calcination of such sample at 700 °C (e) and 900 °C (f). The inset in f is a TEM micrograph of the same sample.

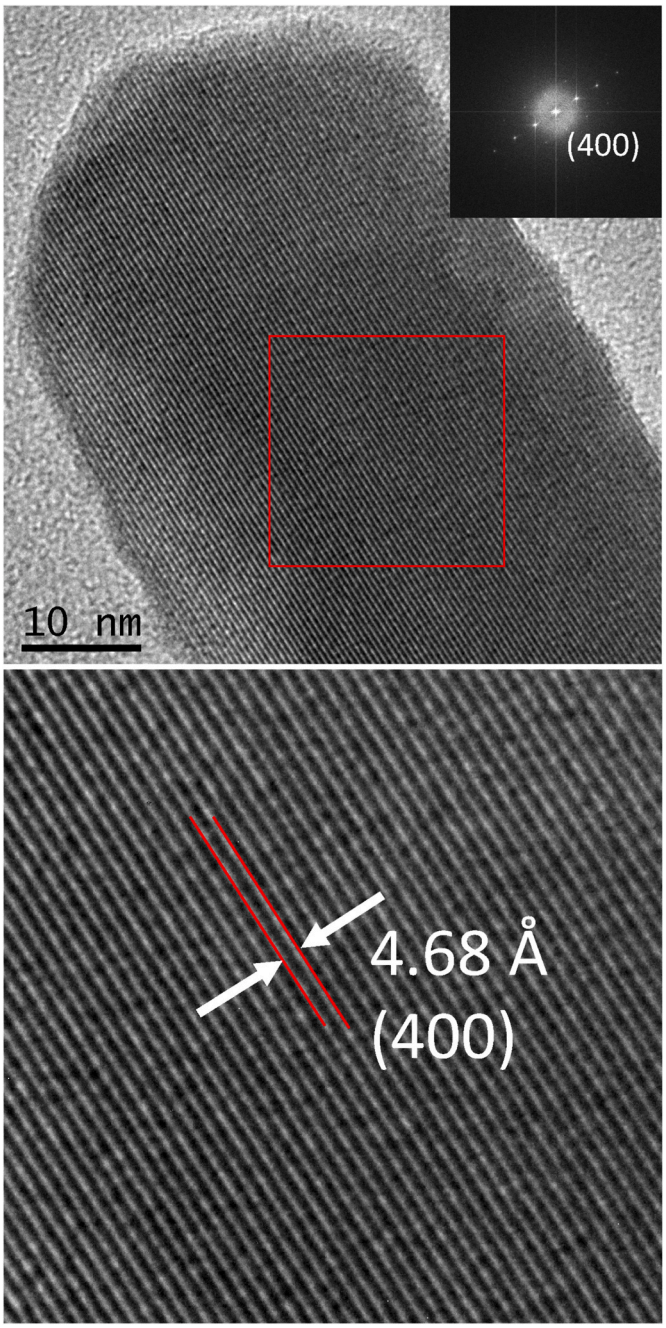

Fig. 6. Top: HREM micrograph of a $MgGeO_3$ nanorod. The inset shows the digital diffraction pattern obtained from the red area. Bottom: Magnification of the red area showing lattice fringes and interplanar distance. (For interpretation of the references to colour in this figure legend, the reader is referred to the Web version of this article.)

Table 1
Nominal and experimental (ICP) Mn^{2+} content and unit cell volume of $MgGeO_3$:x%Mn^{2+} nanorods. The associated errors are given in brackets.

% Mn^{2+} (Nom.)	% Mn^{2+} (Exp.)	Unit cell volume (Å^3)
0.0	0.00	899.09(1)
0.2	0.18	899.24(1)
0.5	0.50	899.42(1)
1.0	1.11	899.91(1)
2.0	2.30	900.83(1)
4.0	4.63	902.78(1)

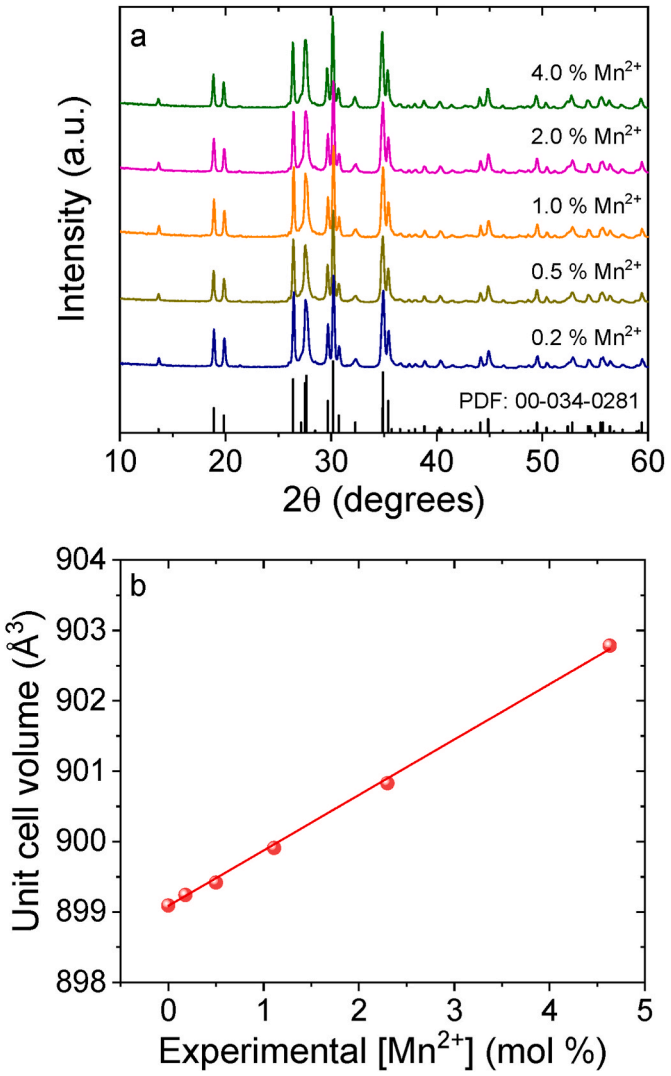

Fig. 7. a) Experimental XRD patterns of $MgGeO_3$:x%Mn^{2+} nanorods. Reflections of orthorhombic $MgGeO_3$ (PDF 00-034-0281) are shown at the bottom. b) Unit cell volume versus experimental Mn^{2+} content of the samples shown in a.

increasing Mn^{2+} content. This shift must result from the expansion of the unit cell as a consequence of the larger size of Mn^{2+} cations (0.83 Å) replacing the smaller Mg^{2+} ones (0.72 Å) in the octahedral sites of the orthorhombic $MgGeO_3$ structure. The unit cell volume values obtained from LeBail refinements are given in Table 1 and plotted versus Mn^{2+} content in Fig. 7b. The cell volume increases linearly with increasing Mn^{2+} content which indicates the effective replacement of Mn^{2+} for Mg^{2+} in the orthorhombic $MgGeO_3$ unit cell.

The excitation photoluminescence spectrum of the $MgGeO_3$:2.0% Mn^{2+} nanorods monitored at 678 nm (Fig. 8a) showed a broad band at $\lambda \leq 350$ nm with maximum below 250 nm that is due to the $^6A_{1g} \rightarrow {}^4A_{1g}$ transition of Mn^{2+} ions. The weak bands in the wavelength range 340–450 nm can be attributed to electron transitions of Mn^{2+} from the $^6A_{1g}$ to the $^4A_{1g}$,^4E_g(G) states [30]. The emission spectrum of the same sample excited at 250 nm exhibited a broad band from around 600 to 850 nm, peaking at 678 nm (Fig. 8b, green line). This emission band is characteristic of Mn^{2+} ions located in an octahedral environment and it is due to the $^4T_{1g} \rightarrow {}^6A_{1g}$ transition [31]. Fig. 8b shows that the emission spectra of the rest of $MgGeO_3$:x%Mn^{2+} nanorods were identical to that of the 2.0% Mn^{2+}-doped sample in terms of bandwidth and position. However, their intensity progressively increased from the sample doped with 0.5% Mn^{2+} up to the sample doped with 2.0% Mn^{2+} and then

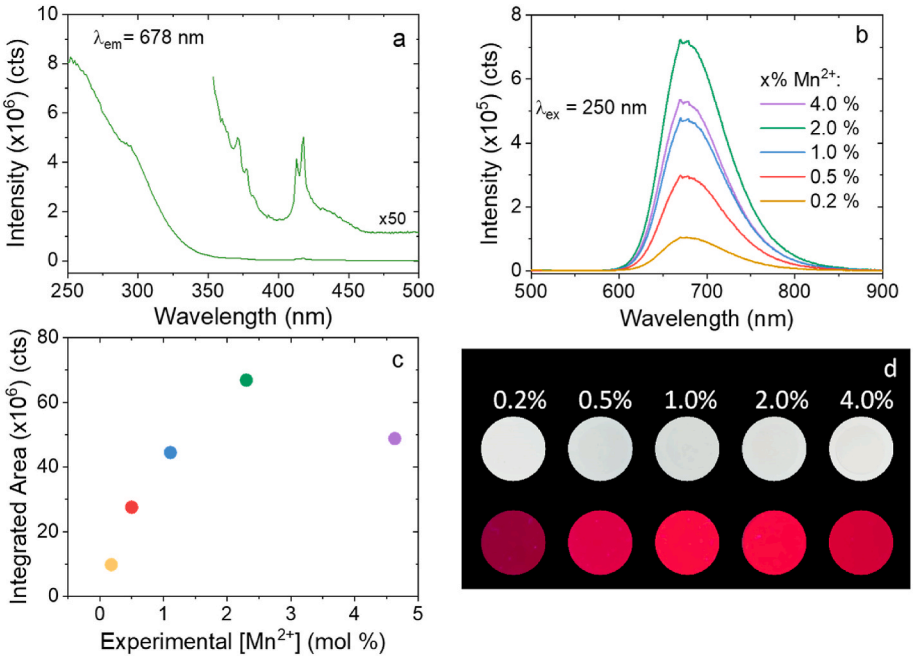

Fig. 8. a) Excitation spectrum recorded on the $MgGeO_3$:2.0%Mn^{2+} nanorods; b) emission spectra of $MgGeO_3$:x%Mn^{2+} nanorods (x = nominal content); c) integrated area of the emission spectra shown in b *vs.* experimental Mn^{2+} content; and d) images of the different $MgGeO_3$:x%Mn^{2+} nanorods under white light (top) and under UV lamp (312 nm) (bottom).

decreased for the 4.0% Mn^{2+}-doped sample. This trend is better observed in Fig. 8c, where the area under the curve of the spectra in Fig. 8b were plotted versus Mn^{2+} content. In summary, the $MgGeO_3$ nanorods doped with 2.0% Mn^{2+} showed the highest emission intensity while concentration quenching effect took place for Mn^{2+} contents between 2.0% and 4.0%. The broad emission band observed under UV excitation is responsible for the red emission of the samples as observed in the digital photographs of Fig. 8d which were taken under white light (top) and under a portable UV lamp (bottom). The bottom photographs agree well with the evolution of the emission intensity observed in Fig. 8b and c with the 2.0% Mn^{2+}-doped sample showing the brightest photoluminescence emission under UV light.

Fig. 9a shows the persistent excitation spectrum obtained after excitation of the $MgGeO_3$:0.5%Mn^{2+} nanorods at the different wavelengths between 250 and 400 nm for 2 min and monitoring the emission at 678 nm. Likewise, Fig. 9b shows the persistent emission spectrum of the same sample obtained after excitation of the powder at 250 nm for 2 min and monitoring the emission between 500 and 900 nm. Both the persistent luminescence excitation and emission spectra, reported here for the first time for the $MgGeO_3$:Mn^{2+} persistent phosphor, have profiles identical to those of the corresponding photoluminescence spectra (Fig. 8b), indicating that the red persistent luminescence originated from the same Mn^{2+} emitting centers.

Fig. 9c shows the persistent luminescence decay curves of $MgGeO_3$:x

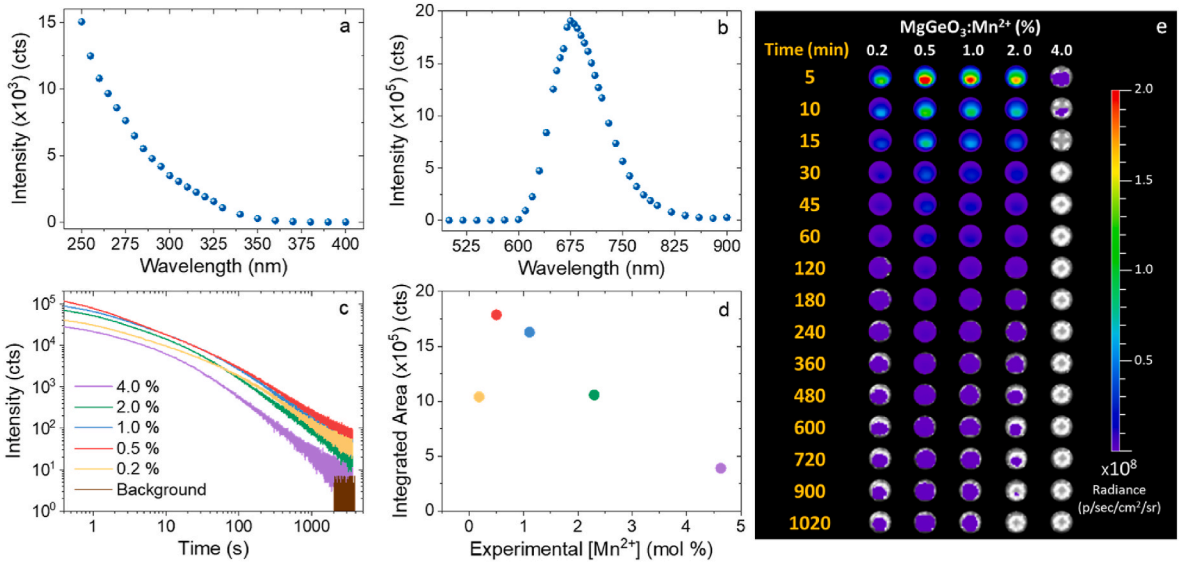

Fig. 9. Persistence excitation spectrum (a) and persistence emission spectrum (b) of $MgGeO_3$:0.5%Mn^{2+} nanorods; c) Persistent luminescence decay curves of $MgGeO_3$:x%Mn^{2+} (x = nominal content) nanorods recorded after illumination with 250 nm light for 5 min; d) Integrated area of the decay curves shown in c *vs.* experimental Mn^{2+} content; e) IVIS Lumina images of the persistent luminescence emitted by $MgGeO_3$:x%Mn^{2+} nanorods recorded at different times after switching off the UV lamp that was on for 5 min for traps charging.

%Mn^{2+} nanorods with different Mn^{2+} doping levels, recorded at an emission wavelength of 678 nm after excitation at 250 nm for 5 min. The same amount of powder was used for each measurement so that the intensity of the curves can be compared to each other. It can be observed that all samples showed emission after stopping the excitation radiation, although the emission intensity varied with the Mn^{2+} doping level. The $MgGeO_3$:0.5%Mn^{2+} sample clearly showed the more intense emission at any time, while the one doped with 4.0% Mn^{2+} always showed the lowest one. To easily evaluate the evolution of the persistent emission with Mn^{2+} content for all samples, we have plotted, in Fig. 9d, the area under the curves of Fig. 9c versus Mn^{2+} doping level. The persistent luminescence intensity increased from the sample doped with 0.2% Mn^{2+} to the one doped with 0.5% Mn^{2+} while higher Mn^{2+} contents gave rise to the decrease of such magnitude. In conclusion, although the optimum Mn^{2+} doping level for the maximum photoluminescence emission was found to be 2.0% Mn^{2+}, a much lower level (0.5% Mn^{2+}) was enough to get the highest persistent emission. Such difference can be explained on the basis of the different mechanisms involved in the photoluminescence and persistent luminescence processes [32]. Photoluminescence emission in $MgGeO_3$:x%Mn^{2+} is caused by direct excitation (with UV light) of Mn^{2+} electrons from the ground energy level $^6A_{1g}$ to the higher excited state $^4A_{1g}$ followed by non-radiative decay to the $^4T_{1g}$ level and radiative red emission from this level to the ground state. Increasing Mn^{2+} content leads to the increase of the photoluminescence emission until concentration quenching takes place. The PersL process is, however, a very different, involving storage of the excitation energy in lattice defects (energy traps), consisting mainly of oxygen vacancies [14] followed by charges release, recombination and luminescence emission from Mn^{2+} ions residing mainly near the traps. This explains why the optimal doping concentration of emitters is usually at a much lower level when compared with the photoluminescence process.

Interestingly, Wang et al. demonstrated that in comparison with the most common high-energy UV lamp used for achieving NIR persistent emission, long-wavelength red light can also induce NIR PersL in $MgGeO_3$:Mn^{2+},Yb^{3+} phosphor through an upconverison charging (UCC) strategy [20]. As a proof of concept, the persistent luminescence curve of our $MgGeO_3$:0.5%Mn^{2+} nanorods was recorded after 10 min irradiation with a 639 nm laser (output power 200 mW) observing an intense NIR PersL (Fig. S5). This excitation strategy can be of interest for bio-applications. Further studies are in progress to analyse the persistent luminescence mechanism after UCC in $MgGeO_3$:Mn^{2+} nanorods.

The effect of Mn^{2+} content on the emission brightness with time can be easily observed in Fig. 9e, that shows the images of persistence luminescence acquired, in an IVIS Lumina, for the $MgGeO_3$:x%Mn^{2+} nanorods at different periods of time after illumination for 5 min with a UV lamp (312 nm). The sample doped with 0.5% Mn^{2+} is the brightest one at any time, in good agreement with the decay curves presented in Fig. 9c. Moreover, Fig. 9e shows that the luminescent signal of the latter was detected for more than 1020 min (17 h), illustrating the excellent persistent luminescent properties of our Mn^{2+}-doped $MgGeO_3$ nanophosphor.

4. Conclusions

A salt-assisted method has been developed for the synthesis of $MgGeO_3$ nanorods, which consists of dissolving GeO_2, $Mg_5(CO_3)_4(OH)_2{\cdot}5H_2O$ and K_2SO_4 in water, followed by evaporation to dryness and further calcination of the dried powder. Crystallization of $MgGeO_3$ was observed at 700 °C, a remarkably lower temperature than that required by conventional solid-sate reaction (≥1100 °C). This behaviour is ascribed to the formation of a layered Mg–Ge oxide hydrate during the drying stage in which, the Ge and Mg cations are intimately mixed thus favouring the diffusion processes required for $MgGeO_3$ crystallization. Moreover, this method allows to control particle shape and size producing, after calcination at 900 °C, particles with uniform shape (nanorods) and a mean size of 350 nm × 99 nm. By adding a Mn^{2+} precursor to the starting solution, the proposed method yields Mn^{2+}-doped $MgGeO_3$ nanophosphors with the same morphological and structural characteristics as the undoped sample. Noticeably, this is the first time in the literature that uniform $MgGeO_3$:Mn^{2+} nanophosphors are reported. The nominal Mn^{2+} doping level giving rise to the maximum photoluminescence emission was found to be 2.0 mol% whereas the sample doped with 0.5 mol% Mn^{2+} showed the best persistent luminescence. The optimum persistent nanophosphors showed an intense red emission, which persisted at least 17 h after stopping excitation. Such excellent properties make the developed nanophosphor an attractive candidate for their use in optical and biotechnological applications.

Declaration of competing interest

The authors declare that they have no known competing financial interests or personal relationships that could have appeared to influence the work reported in this paper.

Acknowledgements

This publication is part of the I + D + I Grant PID2021-122328OB-I00 funded by MCIN/AEI/10.13039/501100011033 and by "ERDF A way of making Europe". E.A. acknowledges Grant FPU19/00527 funded by MCIN/AEI/10.13039/501100011033 and by "ESF Investing in your future".

Appendix A. Supplementary data

Supplementary data to this article can be found online at https://doi.org/10.1016/j.ceramint.2023.09.008.

References

[1] Y. Li, M. Gecevicius, J. Qiu, Long persistent phosphors-from fundamentals to applications, Chem. Soc. Rev. 45 (8) (2016) 2090–2136, https://doi.org/10.1039/c5cs00582e.
[2] J. Xu, S. Tanabe, Persistent luminescence instead of phosphorescence: history, mechanism, and perspective, J. Lumin. 205 (2019) 581–620, https://doi.org/10.1016/j.jlumin.2018.09.047.
[3] K. Huang, et al., Designing next generation of persistent luminescence: recent advances in uniform persistent luminescence nanoparticles, Adv. Mater. 34 (14) (2022), 2107962, https://doi.org/10.1002/adma.202107962.
[4] L. Yang, S.L. Gai, H. Ding, D. Yang, L.L. Feng, P.P. Yang, Recent progress in inorganic afterglow materials: mechanisms, persistent luminescent properties, modulating methods, and bioimaging applications, Adv. Opt. Mater. 11 (2023), https://doi.org/10.1002/adom.202202382. Art no. 2202382.
[5] N. Liu, et al., In vivo repeatedly activated persistent luminescence nanoparticles by radiopharmaceuticals for long-lasting tumor optical imaging, Small 16 (26) (2020), 2001494, https://doi.org/10.1002/smll.202001494.
[6] H.H. Li, S. Yin, Y.H. Wang, T. Sekino, S.W. Lee, T. Sato, Roles of Cr^{3+} doping and oxygen vacancies in $SrTiO_3$ photocatalysts with high visible light activity for NO removal, J. Catal. 297 (2013) 65–69, https://doi.org/10.1016/j.jcat.2012.09.019.
[7] S.X. Lian, et al., Effectively leveraging solar energy through persistent dual red phosphorescence: preparation, characterization, and density functional theory study of $Ca_2Zn_4Ti_{16}O_{38}$:Pr^{3+}, J. Phys. Chem. C 114 (15) (2010) 7196–7204, https://doi.org/10.1021/jp911885c.
[8] L.N. Fu, J. Wang, N. Chen, Q.Q. Ma, D.Q. Lu, Q. Yuan, Enhancement of long-lived luminescence in nanophosphors by surface defect passivation, Chem. Commun. 56 (49) (2020) 6660–6663, https://doi.org/10.1039/d0cc02658a.
[9] Y.X. Zhuang, et al., Trap depth engineering of $SrSi_2O_2N_2$:Ln^{2+},Ln^{3+} (Ln^{2+} = Yb, Eu; Ln^{3+} = Dy, Ho, Er) persistent luminescence materials for information storage applications, ACS Appl. Mater. Interfaces 10 (2) (2018) 1854–1864, https://doi.org/10.1021/acsami.7b17271.
[10] Q. Lin, Z. Li, Q. Yuan, Recent advances in autofluorescence-free biosensing and bioimaging based on persistent luminescence nanoparticles, Chin. Chem. Lett. 30 (9) (2019) 1547–1556, https://doi.org/10.1016/j.cclet.2019.06.016.
[11] S.K. Sun, H.F. Wang, X.P. Yan, Engineering persistent luminescence nanoparticles for biological applications: from biosensing/bioimaging to theranostics, Accounts Chem. Res. 51 (5) (2018) 1131–1143, https://doi.org/10.1021/acs.accounts.7b00619.
[12] S.T. Yang, W.J. Dai, W. Zheng, J. Wang, Non-UV-activated persistent luminescence phosphors for sustained bioimaging and phototherapy, Coord. Chem. Rev. 475 (2023), https://doi.org/10.1016/j.ccr.2022.214913. Art no. 214913.
[13] V. Castaing, E. Arroyo, A.I. Becerro, M. Ocaña, G. Lozano, H. Míguez, Persistent luminescent nanoparticles: challenges and opportunities for a shimmering future,

J. Appl. Phys. 130 (8) (2021), 080902, https://doi.org/10.1063/5.0053283. Art no.
[14] M. Iwasaki, D.N. Kim, K. Tanaka, T. Murata, K. Morinaga, Red phosphorescence properties of Mn ions in MgO-GeO_2 compounds, Sci. Technol. Adv. Mater. 4 (2) (2003) 137–142, https://doi.org/10.1016/s1468-6996(03)00025-1.
[15] N.L. Ross, A. Navrotsky, Study of the $MgGeO_3$ polymorphs (ortho-pyroxene, clinopyroxene, and ilmenite structures) by calorimetry, spectroscopy, and phase-equilibria, Am. Mineral. 73 (11–12) (1988) 1355–1365.
[16] D.T. Palumbo, J.J. Brown, Electronic states of Mn^{2+}-activated phosphors. 1. Green-emitting phosphors, J. Electrochem. Soc. 117 (9) (1970) 1184–1188, https://doi.org/10.1149/1.2407765.
[17] Y. Katayama, J. Ueda, S. Tanabe, Effect of Bi_2O_3 doping on persistent luminescence of $MgGeO_3$:Mn^{2+} phosphor, Opt. Mater. Express 4 (4) (2014) 613–623, https://doi.org/10.1364/ome.4.000613.
[18] Y. Katayama, T. Kayumi, J. Ueda, P. Dorenbos, B. Viana, S. Tanabe, The role of Ln^{3+} (Ln = Eu, Yb) in persistent red luminescence in $MgGeO_3$:Mn^{2+}, J. Mater. Chem. C 5 (34) (2017) 8893–8900, https://doi.org/10.1039/c7tc03151c.
[19] S.H. Zheng, et al., X-ray recharged long afterglow luminescent nanoparticles $MgGeO_3$:Mn^{2+},Yb^{3+},Li^{+} in the first and second biological windows for long-term bioimaging, Nanoscale 12 (26) (2020) 14037–14046, https://doi.org/10.1039/c9nr10622g.
[20] W.L. Wang, et al., A red-light-chargeable near infrared $MgGeO_3$:Mn^{2+},Yb^{3+} persistent phosphor for bioimaging and optical information storage applications, Inorg. Chem. Front. 8 (24) (2021) 5149–5157, https://doi.org/10.1039/d1qi01158h.
[21] A.K.P. Mann, J. Fu, C.J. DeSantis, S.E. Skrabalak, Spatial and temporal confinement of salt fluxes for the shape-controlled synthesis of Fe_2O_3 nanocrystals, Chem. Mater. 25 (9) (2013) 1549–1555, https://doi.org/10.1021/cm3038087.
[22] S.K. Gupta, Y.B. Mao, Recent developments on molten salt synthesis of inorganic nanomaterials: a review, J. Phys. Chem. C 125 (12) (2021) 6508–6533, https://doi.org/10.1021/acs.jpcc.0c10981.
[23] X.J. Wei, et al., Molten salt synthesis of persistent luminescent/magnetic Cr^{3+}-doped zinc gallogermanate particles, J. Phys. Chem. C 127 (7) (2023) 3733–3741, https://doi.org/10.1021/acs.jpcc.2c08045.
[24] X. Xiao, et al., Scalable salt-templated synthesis of two-dimensional transition metal oxides, Nat. Commun. 7 (2016), https://doi.org/10.1038/ncomms11296. Art no. 11296.
[25] B.Y. Yan, et al., Salt powder assisted synthesis of nanostructured materials and their electrochemical applications in energy storage devices, Chem. Eng. J. 400 (2020), https://doi.org/10.1016/j.cej.2020.125895. Art no. 125895.
[26] Y.I. Park, et al., Transformation of hydrophobic iron oxide nanoparticles to hydrophilic and biocompatible maghemite nanocrystals for use as highly efficient MRI contrast agent, J. Mater. Chem. 21 (31) (2011) 11472–11477, https://doi.org/10.1039/c1jm10432b.
[27] A. Pflugmacher, D. Schorning, R. Schwarz, Beitrage zur chemie des germaniums .23. uber aluminiumgermanate, magnesiumgermanate und germaniumultramarine, Zeitschrift Fur Anorganische Und Allgemeine Chemie 295 (1–2) (1958) 93–105, https://doi.org/10.1002/zaac.19582950108.
[28] H. Strese, U. Hofmann, Synthesis of magnesium silicate-gels with two dimensional regular structures, Zeitschrift Fur Anorganische Und Allgemeine Chemie 247 (1/2) (1941) 65–95, https://doi.org/10.1002/zaac.19412470107.
[29] G. Doke, A. Antuzevics, G. Krieke, A. Kalnina, M. Springis, A. Sarakovskis, UV and X-ray excited red persistent luminescence in Mn^{2+} doped $MgGeO_3$ material synthesized in air and reducing atmosphere, J. Lumin. 234 (2021), https://doi.org/10.1016/j.jlumin.2021.117995. Art no. 117995.
[30] T. Sanada, K. Yamamoto, K. Kojima, N. Wada, Red luminescence in MgO-GeO_2 gel glasses and glass ceramics doped with Mn ions prepared by sol-gel method, J. Sol. Gel Sci. Technol. 41 (3) (2007) 237–243, https://doi.org/10.1007/s10971-006-9005-3.
[31] Y. Cong, B. Li, S.M. Yue, L.M. Zhang, W.L. Li, X.J. Wang, Enhanced red phosphorescence in $MgGeO_3$:Mn^{2+} by addition of Yb^{3+} ions, J. Electrochem. Soc. 156 (4) (2009) H272–H275, https://doi.org/10.1149/1.3077570.
[32] R.M. Calderón-Olvera, et al., Persistent luminescence Zn_2GeO_4:Mn^{2+} nanoparticles functionalized with polyacrylic acid: one-pot synthesis and biosensing applications, ACS Appl. Mater. Interfaces 15 (17) (2023) 20613–20624, https://doi.org/10.1021/acsami.2c21735.